nature photonics

Article

https://doi.org/10.1038/s41566-025-01801-2

Measurement of optically induced broken time-reversal symmetry in atomically thin crystals

Received: 4 March 2025

Accepted: 10 October 2025

Published online: 14 November 2025

Check for updates

Florentine Friedrich [1,5], Paul Herrmann [1,5], Shridhar Sanjay Shanbhag [2], Sebastian Klimmer [1,3], Jan Wilhelm [2] & Giancarlo Soavi [1,4]

Time-reversal and space-inversion symmetries are fundamental properties of crystals and play a role in underlying phenomena such as magnetism, topology and non-trivial spin textures. Transition metal dichalcogenides (TMDs) represent an excellent tunable model system to explore the interplay between these symmetries as they can be engineered on demand by tuning the number of layers and via all-optical bandgap modulation. In this work, we modulate and study time-reversal symmetry in mono- and bilayer TMDs with all-optical methods using third-harmonic Faraday rotation. We excite the samples using elliptically polarized light, achieve spin-selective bandgap modulation and consequent breaking of time-reversal symmetry. The reduced symmetry modifies the nonlinear susceptibility tensor, causing a rotation of the emitted third-harmonic polarization. With this method, we probe broken time-reversal symmetry in both non-centrosymmetric (monolayer) and centrosymmetric (bilayer) WS_2 crystals. Furthermore, we discuss how the detected third-harmonic rotation angle directly links to spin-valley locking in monolayer TMDs and spin-valley-layer locking in bilayer TMDs. Our results show a powerful approach to study broken time-reversal symmetry in crystals regardless of space-inversion symmetry, and shed light on the spin, valley and layer coupling of atomically thin semiconductors.

Time-reversal symmetry (TRS), in combination with space-inversion symmetry (SIS), defines the energy-spin properties and the Berry curvature of crystals[1]. Thus, the presence or absence of TRS and SIS is paramount to explain and understand a variety of phenomena in condensed-matter physics, ranging from magnetism[2] to spin-valley locking[3,4], anomalous transport[5,6] and topology[7]. Nonlinear optics (NLO) is an established and powerful tool to investigate the effect of spatial symmetries and TRS breaking in crystals[2,8]. The most relevant example is arguably the study of ferroic materials[2,9–12], where a variety of physical and optical properties are captured by NLO effects described by magnetic point groups[13] (Supplementary Section 1). Among the applications of NLO to the study of time-non-invariant phenomena, second-harmonic nonlinear Kerr/Faraday rotation plays a key role. It has been predicted and experimentally observed that nonlinear Kerr/Faraday rotation offers higher sensitivity compared with its linear counterpart[14,15]. The technique has already been applied to bulk[16,17] and atomically thin crystals[18,19]. However, most measurements so far were limited to non-centrosymmetric crystals, whereas the measurement

[1]Institute of Solid State Physics, Friedrich Schiller University Jena, Jena, Germany. [2]Institute of Theoretical Physics and Regensburg Center for Ultrafast Nanoscopy (RUN), University of Regensburg, Regensburg, Germany. [3]ARC Centre of Excellence for Transformative Meta-Optical Systems, Department of Electronic Materials Engineering, Research School of Physics, The Australian National University, Canberra, Australian Capital Territory, Australia. [4]Abbe Center of Photonics, Friedrich Schiller University Jena, Jena, Germany. [5]These authors contributed equally: Florentine Friedrich, Paul Herrmann. e-mail: giancarlo.soavi@uni-jena.de

https://doi.org/10.1038/s41566-025-01801-2

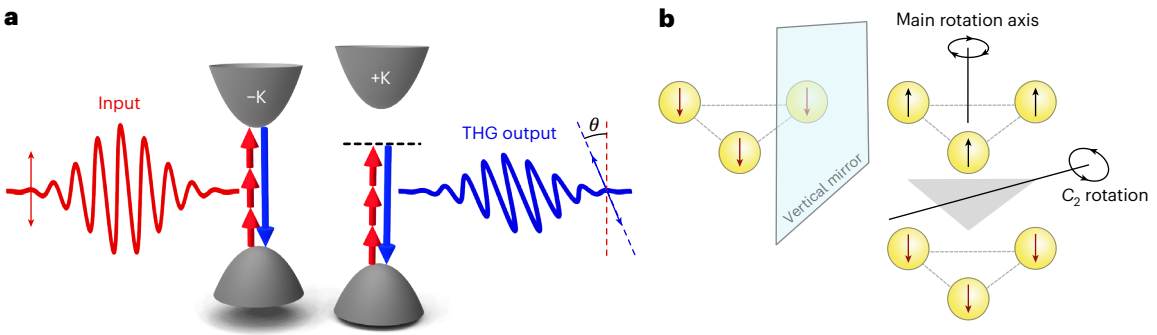

Fig. 1 | Principle of TH Faraday rotation and certain symmetry operations for a spin-oriented three-fold rotational-symmetric system. a, For a monolayer TMD, broken TRS is equivalent to an asymmetry between the ±K valleys. TRS breaking introduces new $\chi^{(3)}$ tensor elements, leading to a rotation of the TH output by angle θ. **b**, Behaviour of a three-fold rotational system with spin-oriented states under the vertical mirror and C_2 rotation. If mirrored vertically, the system changes the spin state from up (straight black arrow pointing upwards) to down (straight red arrow pointing downwards). The same is true for an in-plane two-fold rotation operation (C_2 rotation).

of broken TRS in centrosymmetric crystals remains a challenge. For centrosymmetric crystals, the most common approach to study broken TRS relies on the electric quadrupole response[20], and very recently, another approach has been demonstrated, based on light–matter interactions with engineered topological optical fields to realize room-temperature valleytronics in centrosymmetric systems[21–23]. We propose a different method to study broken TRS in any system, both centrosymmetric and non-centrosymmetric, based on third-harmonic (TH) Faraday rotation. We follow the notation of ref. 24 and define the 'nonlinear Faraday rotation' as the angle between the polarization of the fundamental at frequency ω and the generated Nth harmonic at frequency $N\omega$ for experiments in transmission geometry.

To clarify the operating principle of TH Faraday rotation, we refer to the sketch in Fig. 1a, which depicts the case of a monolayer transition metal dichalcogenide (TMD) with broken SIS. When TRS is preserved, the polarization of the TH signal is parallel to the polarization of the input fundamental beam (FB). For broken TRS, that is, when there is an asymmetry between the ±K points, the TH signal is rotated with respect to the FB, and the degree of broken TRS is proportional to the rotation angle θ. This can be understood in the context of the Curie principle. Any external perturbation reduces the symmetry of a system, allowing only those symmetry operations that are common to both the unperturbed system and the perturbation. Therefore, the new (reduced) symmetry group of the perturbed system can only be a subgroup of the original (unperturbed) crystal class[25]. In our experiments, the perturbation (that is, circularly polarized light) prohibits mirror operations along any plane that contains the propagation axis of the light beam, as well as C_2 rotations perpendicular to the propagation axis of the light beam (Fig. 1b). A careful analysis of all allowed crystallographic (time-reversal-invariant) and magnetic point groups shows that the removal of these symmetry operations is responsible for the TH Faraday rotation. With this simple and direct approach, we detect broken TRS in both monolayer (non-centrosymmetric) and bilayer (centrosymmetric) TMDs. We interpret the results macroscopically, based on the differences between the NLO susceptibilities of crystallographic and magnetic point groups, as well as microscopically, from an analytical model based on the semiconductor Bloch equations for the $\chi^{(3)}$ tensor. With both approaches, we show that broken TRS is induced by off-resonant excitation with circularly polarized light, which is responsible for a spin-selective bandgap opening. This spin-selective off-resonant excitation has different effects in monolayer samples compared with bilayer TMD samples. In monolayer TMDs, the broken SIS leads to spin-valley locking. Thus, off-resonant circularly polarized light creates a valley imbalance by the valley-exclusive optical Stark (OS) and Bloch–Siegert (BS) effects[26,27]. By contrast, in bilayer TMDs, where SIS is preserved, the ±K valleys are spin degenerate, but the same spin couples to opposite layers in the opposite valleys (spin-valley-layer locking)[28]. In this case, spin-selective excitation by circularly polarized light does not create a valley imbalance, but it simultaneously lifts the spin degeneracy in both valleys. This corresponds to an engineered band dispersion in which TRS is broken whereas SIS is preserved. Thus, our results not only define a powerful approach to study broken TRS in both centrosymmetric and non-centrosymmetric crystals, but they also provide a unique tool to investigate the fascinating spin, valley and layer coupling of atomically thin semiconductors, which represent a platform for ultrafast valleytronic logic operations[29].

Symmetry of mono- and bilayer TMDs

TMDs are the ideal platform to investigate the interplay between SIS and TRS. Both properties can be engineered independently by tuning the number of layers (in the 2H phase, an even/odd number of layers possesses/breaks SIS)[30] and via interaction with light[26,27]. In addition, layered materials like TMDs display a strong resonant NLO response[31] despite their atomic thickness, which enables a variety of applications ranging from all-optical[32] and electrical tunability[33,34] to ultrafast logic operations[29,35] and nonlinear valleytronics[36].

Monolayer TMDs belong to the $\bar{6}m2$ crystallographic point group. They are direct-gap semiconductors with optical transitions at the ±K valleys of the Brillouin zone. Since the ±K transitions are mainly defined by the d orbitals of the transition metal atoms[37], we represent the spin states of the lowest-energy transitions on the W sites (Fig. 2). When TRS is preserved, the energy and spin at the valleys must follow $E_{\uparrow}(+\mathbf{k}) = E_{\downarrow}(-\mathbf{k})$, and thus, optical transitions for both spins are energetically degenerate and equally probable (Fig. 2a,c). The stereographic projection (Fig. 2b) shows a summary of the allowed symmetry operations in a monolayer TMD when TRS is preserved (Supplementary Section 2). Breaking of TRS in monolayer TMDs is equivalent to lifting the energy degeneracy between the ±K valleys, thereby making the lowest-energy optical transition allowed for only one spin state (Fig. 2d,f). The symmetry of monolayer TMDs reduces to the $\bar{6}m'2'$ magnetic point group on TRS breaking (Figs. 1b and 2e and Supplementary Sections 1 and 2).

By contrast, 2H-stacked bilayer TMDs belong to the $\bar{3}m$ point group when TRS is preserved. Bilayer TMDs are indirect-gap semiconductors[38], but they still have a direct-gap transition at the ±K valleys. Since both SIS and TRS are preserved, the ±K transition are spin degenerate. In each valley, opposite spins are coupled to opposite layers (Fig. 2i), leading to the so-called spin-valley-layer locking[28]. Breaking of TRS reduces the symmetry of bilayer TMDs to the $\bar{3}m'$ magnetic point group: vertical mirror planes and the C_2 symmetry operations are only allowed in combination with the antisymmetry operation (Fig. 2k shows the stereographic projection and Supplementary Section 2 provides further details). We stress that the breaking of

https://doi.org/10.1038/s41566-025-01801-2

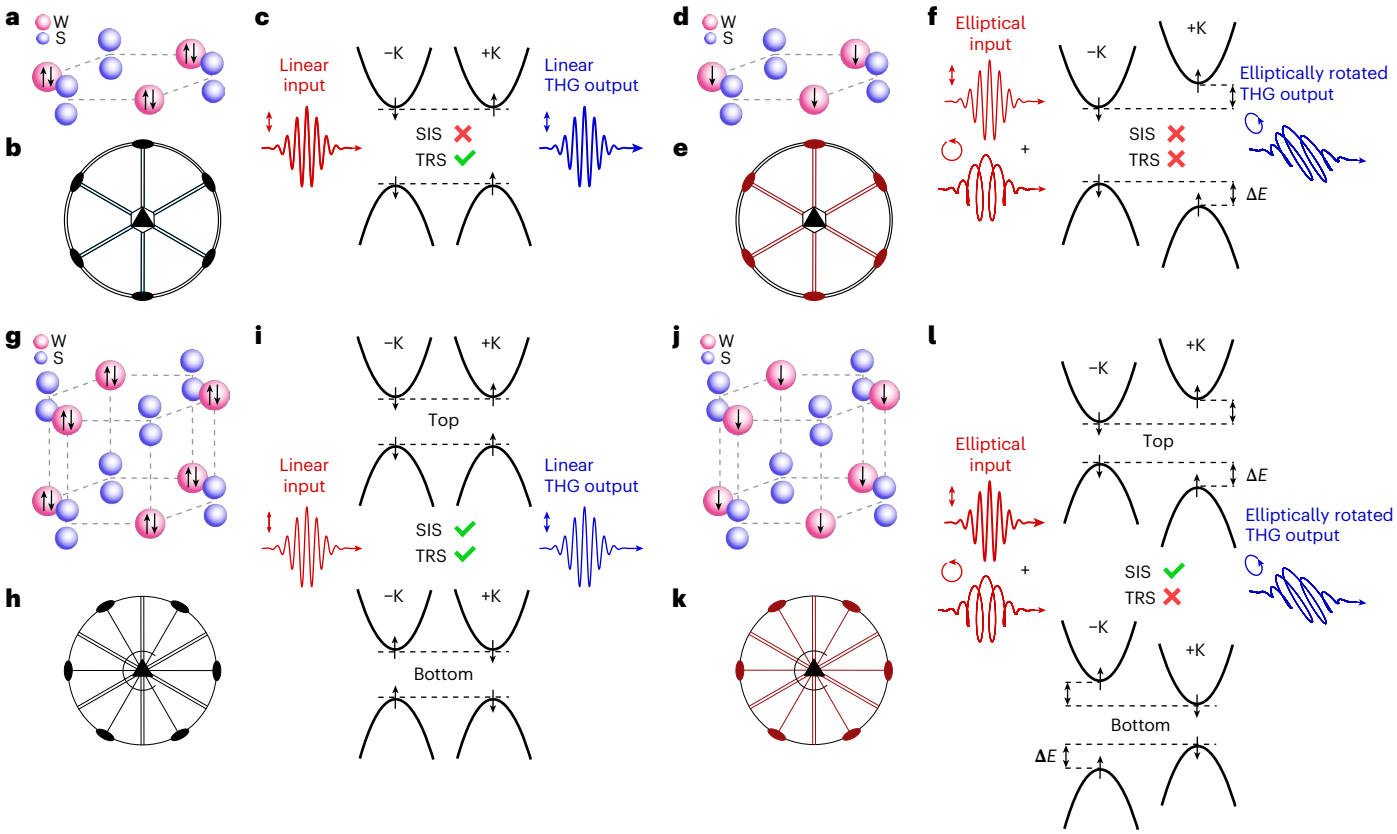

Fig. 2 | Probing TRS breaking in mono- and bilayer WS_2 via TH Faraday rotation. a, Real-space schematic of a WS_2 monolayer with broken SIS and preserved TRS. **b**, Stereographic projection of the $D_{3h} \equiv \bar{6}m2$ crystallographic point group. **c**, Energy and spin of the ±K valleys of a WS_2 monolayer with preserved TRS. Linear excitation leads to linear TH parallel to the input. **d**, Real-space schematic of a WS_2 monolayer with broken SIS and TRS. Due to the spin-selective gap opening, one spin dominates. **e**, Stereographic projection of the $\bar{6}m'2'$ magnetic point group. The red elements represent symmetry operations that are only allowed under antisymmetry. **f**, Energy and spin of the ±K valleys of a WS_2 monolayer with broken TRS. Elliptical excitation leads to the opening of a gap at the +K valley by ΔE and a rotated TH output. **g**, Real-space schematic of a WS_2 bilayer with preserved SIS and TRS. **h**, Stereographic projection of the $D_{3d} \equiv \bar{3}m$ crystallographic point group. **i**, Energy and spin of the ±K valleys of a WS_2 bilayer with preserved TRS. Within one layer, the spin states differ for each valley because of spin-valley-layer locking. Linear excitation leads to linear TH parallel to the input. **j**, Real-space schematic of a WS_2 bilayer with preserved SIS, but broken TRS. Due to spin-selective gap opening, one of the spins is now dominant. **k**, Stereographic projection of the $\bar{3}m'$ magnetic point group. **l**, Energy and spin of the ±K valleys of a WS_2 bilayer with broken TRS. Elliptical excitation leads to the opening of a gap by ΔE in the top and bottom layers and, thus, to a rotated TH output.

TRS in bilayer TMDs is not equivalent to lifting the energy degeneracy between the valleys, but rather to a split between the spin up/down energy levels in both valleys and in opposite layers (Fig. 2l). This effect is responsible for a large degree of circular polarization in photoluminescence (PL) experiments, observed even at room temperature in WS_2 (ref. 39) and $MoSe_2$ (ref. 40).

On the basis of these symmetry considerations (see also Supplementary Section 3), we will now demonstrate that broken TRS can be easily detected as a rotation in the TH polarization with respect to the polarization of the FB in both mono- and bilayer TMDs.

Analytical model and experimental results

TH Faraday rotation in monolayer WS_2

First, we study the non-centrosymmetric WS_2 monolayer. The excitation of TMD monolayers with circularly polarized light is both spin and valley selective[41]. By contrast, linearly polarized light interacts equally with both valleys. Thus, when the FB is linearly polarized and TRS is preserved, the emitted TH signal is linearly polarized and parallel to the input FB (Fig. 2c). The situation changes when an elliptically polarized pulse interacts with the sample, which can be interpreted as a superposition of linearly and circularly polarized light. Although the linearly polarized part has no effect on TRS, the circularly polarized component of the FB creates a valley imbalance by breaking TRS via the valley-selective OS and BS effects[26,41] (Fig. 2f). In this new configuration, the symmetry of the monolayer is reduced to $\bar{6}m'2'$, as discussed above and depicted in Fig. 2e. This symmetry reduction is equivalent to a modification of the $\boldsymbol{\chi}^{(3)}$ tensor. In addition to the time-invariant so-called intrinsic $\chi^{(3)}_{\mathrm{int}}$ elements, corresponding to the unperturbed $\bar{6}m2$ point group, time-non-invariant $\chi^{(3)}_{\mathrm{TRS}}$ elements induced by the broken TRS appear. As we show in detail in Supplementary Section 4, the presence of these additional elements leads to a rotation θ of the TH polarization compared with the unperturbed case, when assuming normal incidence of the electromagnetic field on the sample and within the electric dipole approximation, according to

$$\tan 2\theta = 2\,\frac{\mathrm{Re}\left(\chi^{(3)}_{\mathrm{int}}\chi^{(3)*}_{\mathrm{TRS}}\right)}{\left|\chi^{(3)}_{\mathrm{TRS}}\right|^2 - \left|\chi^{(3)}_{\mathrm{int}}\right|^2} \approx -2\,\frac{\mathrm{Im}\left(\chi^{(3)}_{\mathrm{TRS}}\right)}{\mathrm{Im}\left(\chi^{(3)}_{\mathrm{int}}\right)}, \qquad (1)$$

where * denotes the complex conjugate. Here we have assumed $|\chi^{(3)}_{\mathrm{TRS}}| \ll |\chi^{(3)}_{\mathrm{int}}|$ and $\mathrm{Re}\,(\chi^{(3)}_{\mathrm{int}}) = \mathrm{Re}\,(\chi^{(3)}_{\mathrm{TRS}}) = 0$ at resonance (Supplementary Sections 4 and 5).

To gain a deeper understanding of the microscopic mechanisms of TRS breaking, we use analytical expressions for $\chi^{(3)}_{\mathrm{int}}$ and $\chi^{(3)}_{\mathrm{TRS}}$ derived

https://doi.org/10.1038/s41566-025-01801-2

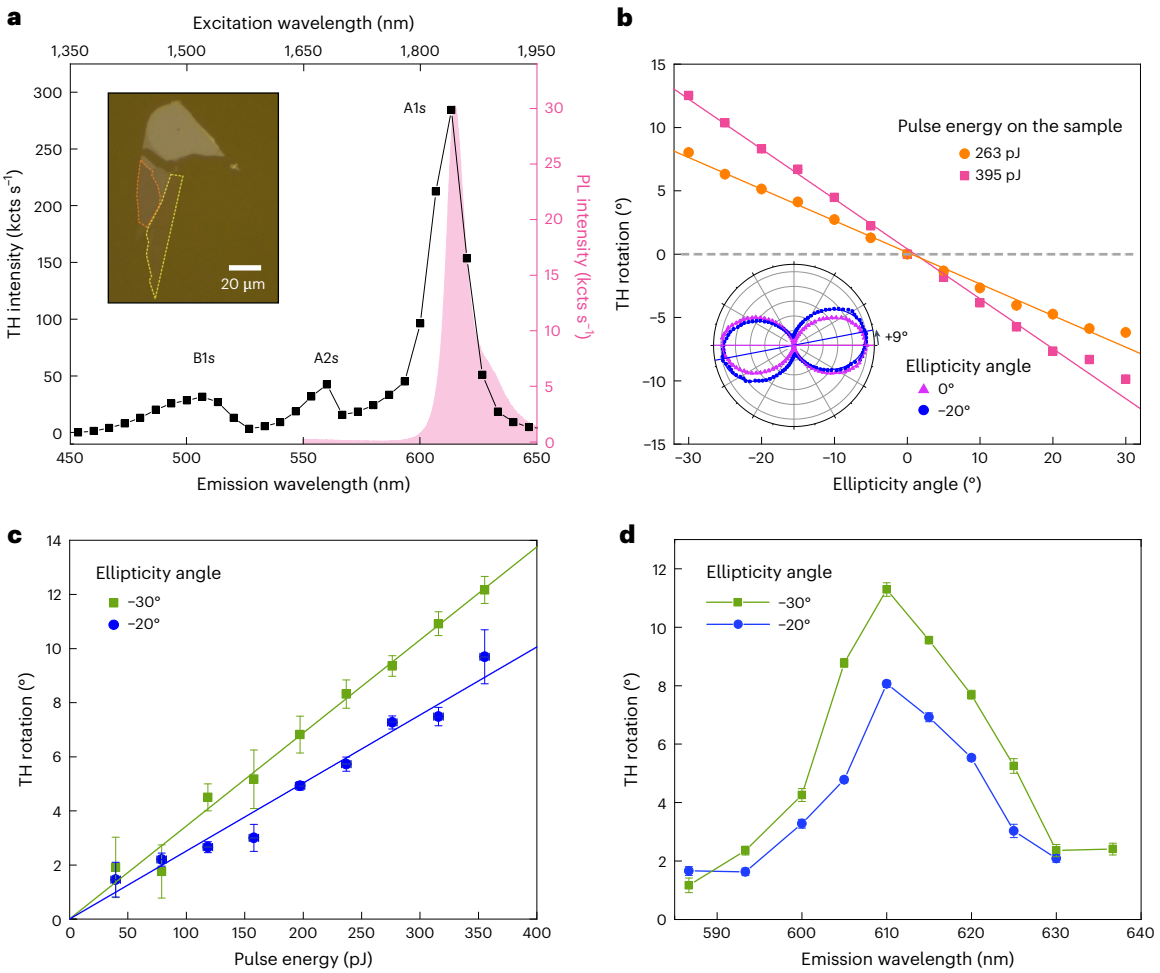

Fig. 3 | PL and TH rotation measurements for different ellipticities and pulse energies in monolayer WS_2. a, Comparison of the total emitted TH intensity for linear fundamental polarization (black squares, left axis) as a function of FB wavelength and the emitted PL (pink line, right axis). The inset shows an optical microscopy image of the used WS_2 sample with the mono- and bilayer regions marked by dotted yellow and orange lines, respectively. **b**, TH rotation angle as a function of the FB ellipticity angle and for an excitation pulse energy of 263 pJ (orange circles) and 395 pJ (pink squares). The solid lines are linear fits to the data. The inset shows the elliptical polarization pattern of the emitted TH for linear (violet triangles) and elliptical (blue circles) input polarization. **c**, Pulse energy dependence of the TH rotation for −20° (blue circles) and −30° (green squares). The solid lines are linear fits to the data with a fixed intercept of 0° rotation at 0 pJ. **d**, Wavelength dependence of the TH rotation angle for an input pulse energy of 395 pJ for ellipticity angles of −20° (blue circles) and −30° (green squares). Data in **b**–**d** are presented as mean values ± regression standard error.

from the semiconductor Bloch equations[41–43]. The expressions depend on the band structure and dipole matrix elements, which we obtain from a two-band TMD monolayer Hamiltonian including the OS and BS shift that break TRS[41]. The final analytical expressions for $\chi^{(3)}_{\mathrm{int}}$ and $\chi^{(3)}_{\mathrm{TRS}}$ are given in Supplementary Section 6, and we use them to evaluate the TH rotation θ from equation (1) as

$$\tan 2\theta = -\frac{2}{1+(2\Delta-3\hbar\omega)^2/(\hbar/T_2)^2}\frac{\Delta E}{\hbar/T_2} \tag{2}$$

$$= -\frac{3}{16}\sin 2\alpha\,\frac{1}{1+(2\Delta-3\hbar\omega)^2/(\hbar/T_2)^2}\frac{\mathcal{E}^2 d^2}{\hbar\Delta/T_2}. \tag{3}$$

Here Δ is the onsite energy (2Δ is the optical gap), α is the ellipticity angle of the polarization ellipse of the FB, T_2 is the dephasing time, ω is the frequency of the beam and ΔE is the difference of the OS and BS shifts between the two valleys (Fig. 2). ΔE is proportional to the square of field strength $\mathcal{E}$ and the absolute value of the transition dipole moment (d), which is identical in the two valleys.

We can now compare our theoretical model with experimental results for monolayer WS_2 (Fig. 3). The WS_2 sample (Methods) shown in Fig. 3a (inset) consists of a mono-/bilayer region (marked in yellow/orange). Since the breaking of TRS is expected to mainly manifest at optical resonances[41] (see equation (3): $2\Delta = 3\hbar\omega$), we first perform PL and TH wavelength dependence to identify these resonances. For the TH wavelength dependence, the FB is linearly polarized. We find the A1s excitonic resonance at 615 nm (Fig. 3a), where we notice a slight blueshift of the TH resonance compared with the PL emission. This can be ascribed to a valley-symmetric bandgap opening in the case of excitation with linearly polarized light[44,45], which modulates the bandgap without breaking TRS. In all the following experiments (Methods), the TH rotation angle is measured by rotating a polarizer in front of the detector to obtain a polarization-dependent pattern for the TH signal, as shown in Fig. 3b (inset) for two example ellipticity angles of 0° (linearly polarized) and −20° (elliptically polarized). Further examples of polarization patterns are provided in Supplementary Section 7. The polarization-dependent TH patterns are fitted with a $\cos^2$ function, from which we obtain the rotation angle θ and the error of the numerical fitting. We fix the wavelength of the FB at 1,830 nm to work close to the A1s resonance, and perform two different sets of experiments: (1) we

https://doi.org/10.1038/s41566-025-01801-2

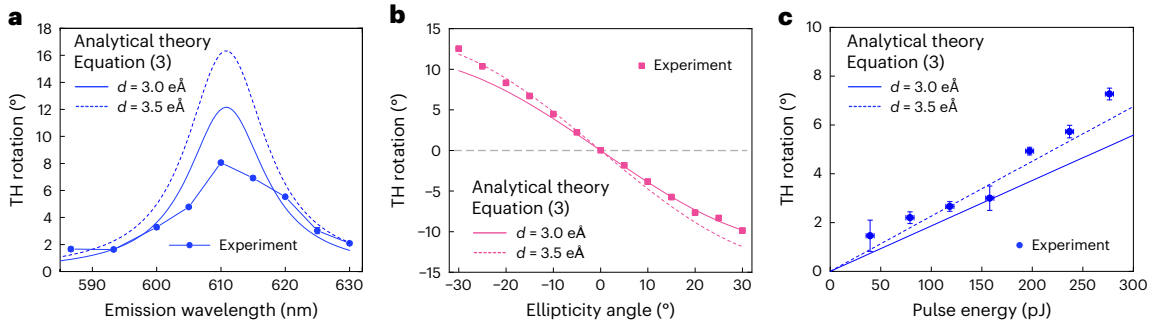

Fig. 4 | Comparison of analytical model and experimental results for monolayer WS_2. a, Wavelength-dependent TH rotation for a fixed ellipticity of −20° and an input pulse energy of 395 pJ (Fig. 3d, blue circles). **b**, Ellipticity-dependent TH rotation for a fixed input pulse energy of 395 pJ (Fig. 3b, pink squares). **c**, Pulse energy-dependent TH rotation for a fixed ellipticity of −20° (Fig. 3c, blue circles). For the analytical calculations, we use $T_2 = 28$ fs, $\Delta = 1.05$ eV and two values of the dipole element, namely, $d = 3$ eÅ (solid lines) and $d = 3.5$ eÅ (dashed lines). Data are presented as mean values ± regression standard error.

fix the input pulse energy and tune the ellipticity of the input FB by rotating a quarter-wave plate in front of the sample (Fig. 3b); (2) we fix the ellipticity and tune the input pulse energy (Fig. 3c). In addition, we scan the wavelength across the A1*s* resonance with fixed pulse energy and ellipticity (Fig. 3d).

For the first type of experiments (Fig. 3b), we observe a clear rotation of the main axis of the polarization ellipse, which can be explained by the new elements of the NLO susceptibility due to broken TRS, as discussed above. The TH rotation angle scales linearly with FB ellipticity: a larger circular component of the FB enhances the effect of TRS breaking. We note that circular THG is forbidden by angular momentum conservation[46], and the total TH intensity scales with the $\cos^2$ of ellipticity. Thus, since the TH intensity decreases drastically for increasing ellipticity of the FB beam, we investigate the TH rotation only up to an ellipticity angle of ±30°.

In the second set of experiments, we fix the ellipticity angle to −30° and −20° and scan the input pulse energy in the range from 40 pJ to 355 pJ. The results are shown in Fig. 3c, where we observe a close-to-linear dependence of the TH rotation angle with respect to the input pulse energy, as expected for TRS breaking due to OS and BS shifts[41]. We highlight that in the fitting shown in Fig. 3c, we fixed the intercept to zero, because the TH rotation must be zero for an unperturbed sample. Finally, we measure the wavelength dependence of the TH rotation angle close to exciton resonance for two different ellipticity angles of −20° and −30° and a fixed input pulse energy of 395 pJ on the sample (Fig. 3d). We observe the largest TH rotation for excitation at the A1*s* resonance, whereas the rotation angle decreases for off-resonant wavelengths. We further note that even though the TH intensity close to resonances can be affected by bandgap modulations that preserve TRS (for example, excitation with linearly polarized light[44,45]), the TH Faraday rotation only measures those changes in the bandgap that effectively break TRS.

Next, we quantitatively compare the experimental results with the analytical equation (3) in Fig. 4. According to equation (3), the TH rotation θ depends on the ellipticity angle α, frequency ω and field strength $\mathcal{E}$ of the FB. Furthermore, θ also depends on the material parameters: optical gap 2Δ, dipole element d and dephasing time T_2. To determine 2Δ and T_2, we focus on the peak of $\theta(\omega)$ in equation (3) at the TH resonance, where $3\omega = 2\Delta$. From the peak position of ~615 nm in the wavelength scan (Fig. 4a), we extract $2\Delta = 2.1$ eV and from the linewidth of the peak, we obtain $T_2 = 28$ fs. We note that the theoretical model only includes dephasing mechanisms such as electron–electron and electron–phonon scattering, leading to a homogeneous broadening. However, the experiments are sensitive to any homogeneous and inhomogeneous broadening mechanism, including space-local bandgap modulations caused by defects and strain[47]. Our extracted value of $T_2 = 28$ fs effectively includes all of these broadening mechanisms.

After determining Δ and T_2, we report the TH rotation θ from equation (3) for two values of the dipole element, namely, $d = 3.0$ eÅ and $d = 3.5$ eÅ. The theoretical and experimental results show good agreement in their wavelength dependence, with peak heights matching within a factor of two (Fig. 4a). For the ellipticity dependence (Fig. 4b), the analytical model gives a nonlinear curve that describes the experimental results with excellent accuracy. The deviation from linear dependence, which we use for simplicity in Fig. 3b, can be understood from the $\sin 2\alpha$ dependence in equation (3), assuming a small θ such that $\tan\theta \approx \theta \propto \sin 2\alpha$. Similarly, we find a linear increase in θ with the fundamental pulse energy both in experiment and in the analytical model (via $\mathcal{E}^2$ in equation (3); Fig. 4c).

TH Faraday rotation in centrosymmetric bilayer WS_2

We now demonstrate the possibility to probe broken TRS in centrosymmetric bilayer WS_2. The breaking of TRS in TMD bilayers follows a similar principle as in the monolayer case (Fig. 2g–l): an elliptical input pulse leads to alternating gap opening (in the +K valley of the upper layer and −K valley of the bottom layer) due to spin-valley-layer locking[28] (Fig. 2l). When TRS is broken, the valleys remain energetically degenerate, but they are no longer spin degenerate. This can be understood by considering the energy spin relation of a system where SIS is preserved ($E_\uparrow(+\mathbf{k}) = E_\uparrow(-\mathbf{k})$) and TRS is broken ($E_\uparrow(+\mathbf{k}) \neq E_\downarrow(-\mathbf{k})$). Looking at the magnetic point groups, bilayer TMDs belong to $\bar{3}m/\bar{3}m'$ when TRS is preserved/broken. These point groups have the same in-plane components of the $\chi^{(3)}$ susceptibility as the $\bar{6}m2/\bar{6}m'2'$ of monolayer TMDs (when TRS is preserved/broken). Thus, for in-plane excitation of the sample, we can apply exactly the same considerations done for monolayer TMDs also to the case of bilayer TMDs. We thus performed the same set of experiments discussed in Fig. 3 also for a bilayer WS_2 crystal (Fig. 5).

We start with PL and TH wavelength dependence to determine the ±K direct transitions of the WS_2 bilayer (Fig. 5a). The PL signal shows two maxima, which we assign to the momentum-direct and phonon-assisted momentum-indirect transitions[42,48,49] at 635 nm and 705 nm, respectively. Momentum-indirect transitions cannot be probed by coherent and parametric harmonic generation, as they require the exchange of momentum with, for example, defects or phonons. For an emission wavelength of 625 nm (FB at 1,875 nm), we observe the maximum TH and assign the difference between PL and TH measurements to the valley and spin-symmetric bandgap modulation induced by linearly polarized light[44,45]. In our TH experiments, we will study only the momentum-direct ±K transitions at an FB wavelength of 1,875 nm.

In analogy with the monolayer case, the ellipticity dependence (Fig. 5b) shows a close-to-linear dependence of the TH rotation angle versus the FB ellipticity. The TH rotation in the case of bilayer WS_2

https://doi.org/10.1038/s41566-025-01801-2

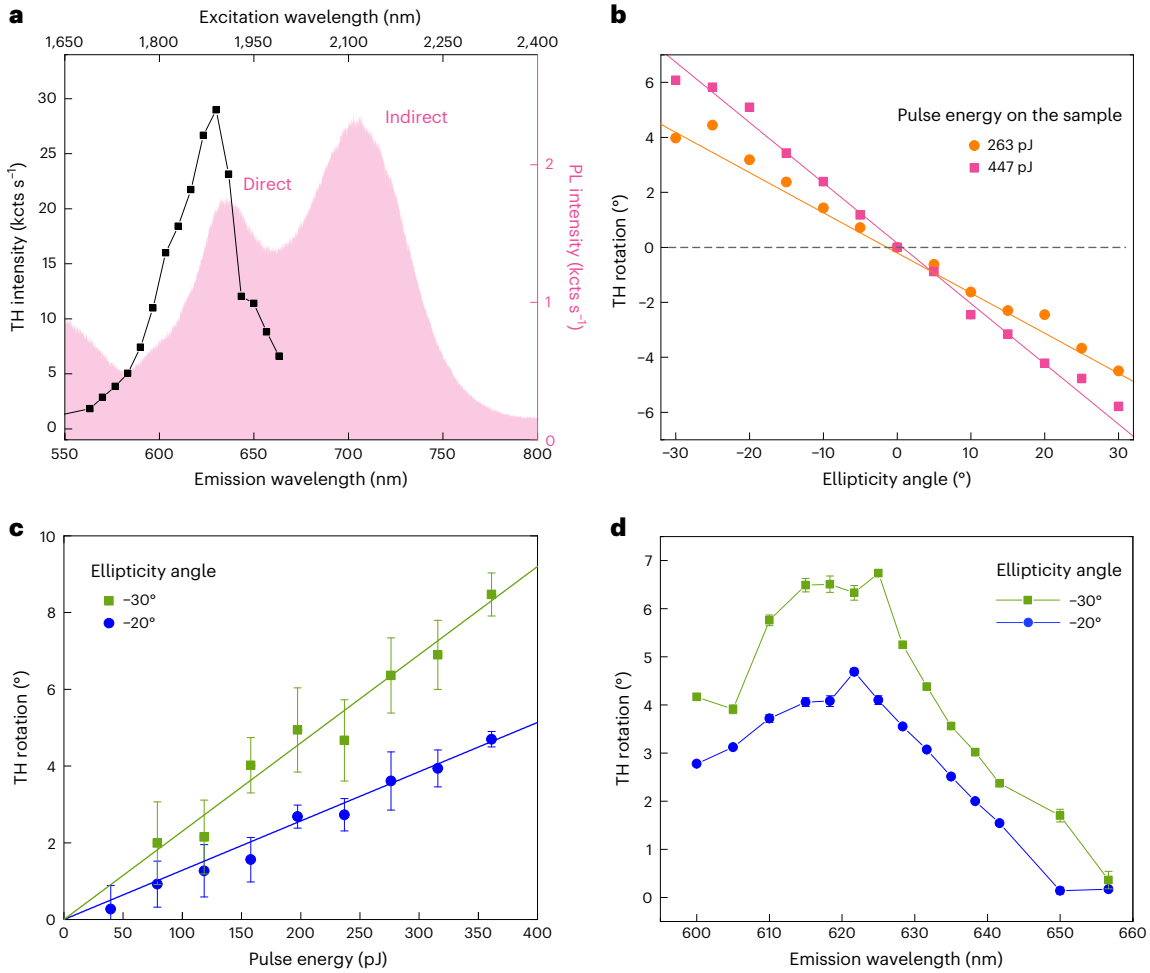

Fig. 5 | PL and TH rotation measurements for different ellipticity angles and pulse energy values in bilayer WS_2. a, Comparison of the total emitted TH intensity (black squares, left axis) and the emitted PL for linear fundamental polarization (pink line, right axis) as a function of the excitation wavelength. **b**, Rotation of the emitted TH dependent on the ellipticity angle and for an excitation pulse energy of 263 pJ (orange circles) and 447 pJ (pink squares). The solid lines are linear fits to the data. **c**, Pulse energy dependence of the TH rotation for −20° (blue circles) and −30° (green squares). The solid lines are linear fits to the data with a fixed intercept of 0° rotation at 0 pJ. **d**, Wavelength dependence of the TH rotation for an input pulse energy of 395 pJ for ellipticity angles of −20° (blue circles) and −30° (green squares). Data in **b**–**d** are presented as mean values ± regression standard error.

follows the same rules discussed in the previous paragraph. Next, we study the pulse energy dependence of the TH rotation angle (Fig. 5c) for different ellipticity angles (−20° and −30°, shown as blue circles and green squares, respectively). We observe a close-to-linear dependence, which is again a clear indication that even in bilayer TMDs, broken TRS, for our experimental conditions, arises from all-optical bandgap modulation. Finally, we measure the wavelength dependence of the TH rotation angle for two different ellipticity angles of −20° and −30° and input pulse energy of 395 pJ (Fig. 5d). We observe the largest TH rotation for excitation at 625 nm, that is, at resonance with the momentum-direct ±K optical transitions.

All these experimental findings agree with our analytical model for bilayer WS_2, which shows that both valleys contribute equally to the TH rotation. The model (Supplementary Section 6) gives a TH rotation angle for the bilayer of

$$\tan 2\theta = -\frac{2}{1+(2\Delta-3\hbar\omega)^2/(\hbar/T_2)^2}\frac{\Delta_{\mathrm{BL}}^{\uparrow/\downarrow}}{\hbar/T_2} \quad (4)$$

$$= -\frac{3}{16}\sin 2\alpha\,\frac{1}{1+(2\Delta-3\hbar\omega)^2/(\hbar/T_2)^2}\frac{\mathcal{E}^2 d^2}{\hbar\Delta/T_2}. \quad (5)$$

This expression is almost identical to equation (3) obtained in the case of monolayer TMDs, with the main difference that the spin-valley-exclusive bandgap modulation of monolayer TMDs (that is, ΔE) is substituted by the valley-symmetric but spin-layer-selective bandgap modulation (that is, $\Delta_{\mathrm{BL}}^{\uparrow/\downarrow}$) in the case of bilayer TMDs. Besides, the primary parametric difference between mono- and bilayer samples is the dephasing time T_2, which is shorter in the bilayer, an indirect-gap semiconductor with additional non-radiative decay channels compared with the monolayer. As a result, the model in equations (3) and (5) predicts a reduced TH rotation θ_{res} at the TH resonance, since $\tan 2\theta_{\mathrm{res}} \propto T_2$. This prediction aligns with our experimental observations, where the TH rotation in the bilayer is approximately half compared with that of the monolayer. Finally, we note that even the interlayer coupling (which we neglect in our model, being smaller compared with the spin–orbit coupling in W-based TMDs[37]) could play a role in explaining the lower TH rotation of bilayer compared with monolayer samples.

Conclusion

We have demonstrated an all-optical method to probe broken TRS in both centrosymmetric and non-centrosymmetric systems. The approach is based on the measurement of TH Faraday rotation, that is, a rotation of the TH polarization angle with respect to the polarization of the input FB. We realize and test TH Faraday rotation in two example

crystals: monolayer WS_2 for the non-centrosymmetric case and bilayer WS_2 for the centrosymmetric case. In both systems, a broken TRS has fundamental implications for the understanding of the light-modulated band structure as well as for technological applications. For monolayers, broken TRS induces a valley imbalance, which could be the source of information for valleytronic operations. In bilayer TMDs, broken TRS interacts with spin-valley-layer locking, which is unique for this type of layered van der Waals structures. For both samples, we show that broken TRS is induced by all-optical and ultrafast energy spin modulation, and the effect is probed by a sizeable TH rotation angle up to 12.5° under our experimental conditions. These results represent an important step towards the development of new all-optical diagnostic techniques to probe broken TRS in any system, regardless of SIS. In addition, this work provides a viable approach for the realization of all-optical and ultrafast valleytronic devices.

Online content

Any methods, additional references, Nature Portfolio reporting summaries, source data, extended data, supplementary information, acknowledgements, peer review information; details of author contributions and competing interests; and statements of data and code availability are available at https://doi.org/10.1038/s41566-025-01801-2.

References

1. Soavi, G. & Wilhelm, J. The signature of topology in polar and chiral non-magnetic crystal classes. Preprint at https://arxiv.org/abs/2501.03684 (2025).
2. Fiebig, M. *Nonlinear Optics on Ferroic Materials* (Wiley, 2023).
3. Xiao, D., Liu, G.-B., Feng, W., Xu, X. & Yao, W. Coupled spin and valley physics in monolayers of MoS_2 and other group-VI dichalcogenides. *Phys. Rev. Lett.* **108**, 196802 (2012).
4. Mak, K. F., He, K., Shan, J. & Heinz, T. F. Control of valley polarization in monolayer MoS_2 by optical helicity. *Nat. Nanotechnol.* **7**, 494–498 (2012).
5. von Klitzing, K. Quantized hall effect. *J. Magn. Magn. Mater.* **31–34**, 525–529 (1983).
6. McIver, J. W. et al. Light-induced anomalous Hall effect in graphene. *Nat. Phys.* **16**, 38–41 (2020).
7. Bao, C., Tang, P., Sun, D. & Zhou, S. Light-induced emergent phenomena in 2D materials and topological materials. *Nat. Rev. Phys.* **4**, 33–48 (2022).
8. Gopalan, V. & Litvin, D. B. Rotation-reversal symmetries in crystals and handed structures. *Nat. Mater.* **10**, 376–381 (2011).
9. Denev, S. A., Lummen, T. T. A., Barnes, E., Kumar, A. & Gopalan, V. Probing ferroelectrics using optical second harmonic generation. *J. Am. Ceram. Soc.* **94**, 2699–2727 (2011).
10. Fiebig, M., Lottermoser, T., Meier, D. & Trassin, M. The evolution of multiferroics. *Nat. Rev. Mater.* **1**, 16046 (2016).
11. Kumar, A. et al. Linear and nonlinear optical properties of $BiFeO_3$. *Appl. Phys. Lett.* **92**, 121915 (2008).
12. Fiebig, M., Fröhlich, D., Krichevtsov, B. B. & Pisarev, R. V. Second harmonic generation and magnetic-dipole-electric-dipole interference in antiferromagnetic Cr_2O_3. *Phys. Rev. Lett.* **73**, 2127–2130 (1994).
13. Guccione, R. On the construction of the magnetic space groups. *Phys. Lett.* **5**, 105–107 (1963).
14. Pustogowa, U., Hübner, W. & Bennemann, K. Enhancement of the magneto-optical Kerr rotation in nonlinear optical response. *J. Magn. Magn. Mater.* **148**, 269–272 (1995).
15. Koopmans, B., Koerkamp, M. G., Rasing, T. & van den Berg, H. Observation of large Kerr angles in the nonlinear optical response from magnetic multilayers. *Phys. Rev. Lett.* **74**, 3692–3695 (1995).
16. Zvezdin, A. Non-linear surface Kerr effect and SHG in magnets. *Physica A* **241**, 444–449 (1997).
17. Ogawa, Y. et al. Magnetization-induced second harmonic generation in a polar ferromagnet. *Phys. Rev. Lett.* **92**, 047401 (2004).
18. Wu, S. et al. Extrinsic nonlinear Kerr rotation in topological materials under a magnetic field. *ACS Nano* **17**, 18905–18913 (2023).
19. Kabos, P., Kos, A. B. & Silva, T. J. Vectorial second-harmonic magneto-optic Kerr effect measurements. *J. Appl. Phys.* **87**, 5980–5982 (2000).
20. Ahn, Y. et al. Electric quadrupole second-harmonic generation revealing dual magnetic orders in a magnetic Weyl semimetal. *Nat. Photon.* **18**, 26–31 (2024).
21. Mrudul, M. S., Jiménez-Galán, A., Ivanov, M. & Dixit, G. Light-induced valleytronics in pristine graphene. *Optica* **8**, 422–427 (2021).
22. Mitra, S. et al. Light-wave-controlled Haldane model in monolayer hexagonal boron nitride. *Nature* **628**, 752–757 (2024).
23. Tyulnev, I. et al. Valleytronics in bulk MoS_2 with a topologic optical field. *Nature* **628**, 746–751 (2024).
24. Matsubara, M., Schmehl, A., Mannhart, J., Schlom, D. G. & Fiebig, M. Giant third-order magneto-optical rotation in ferromagnetic EuO. *Phys. Rev. B* **86**, 195127 (2012).
25. Curie, P. Sur la symétrie dans les phénomènes physiques, symétrie d'un champ électrique et d'un champ magnétique. *J. Phys. Theor. Appl.* **3**, 393–415 (1894).
26. Sie, E. J. et al. Large, valley-exclusive Bloch-Siegert shift in monolayer WS_2. *Science* **355**, 1066–1069 (2017).
27. Kim, J. et al. Ultrafast generation of pseudo-magnetic field for valley excitons in WSe_2 monolayers. *Science* **346**, 1205–1208 (2014).
28. Jones, A. M. et al. Spin–layer locking effects in optical orientation of exciton spin in bilayer WSe_2. *Nat. Phys.* **10**, 130–134 (2014).
29. Gucci, F. et al. Ultrafast valleytronic logic operations. Preprint at https://arxiv.org/abs/2412.08318 (2024).
30. Zhang, Y. et al. Direct observation of the transition from indirect to direct bandgap in atomically thin epitaxial $MoSe_2$. *Nat. Nanotechnol.* **9**, 111–115 (2014).
31. Dogadov, O., Trovatello, C., Yao, B., Soavi, G. & Cerullo, G. Parametric nonlinear optics with layered materials and related heterostructures. *Laser Photon. Rev.* **16**, 2100726 (2022).
32. Klimmer, S. et al. All-optical polarization and amplitude modulation of second-harmonic generation in atomically thin semiconductors. *Nat. Photon.* **15**, 837–842 (2021).
33. Ghaebi, O. et al. Ultrafast opto-electronic and thermal tuning of third-harmonic generation in a graphene field effect transistor. *Adv. Sci.* **11**, 2401840 (2024).
34. Soavi, G. et al. Broadband, electrically tunable third-harmonic generation in graphene. *Nat. Nanotechnol.* **13**, 583–588 (2018).
35. Li, Y. et al. Nonlinear co-generation of graphene plasmons for optoelectronic logic operations. *Nat. Commun.* **13**, 3138 (2022).
36. Herrmann, P. et al. Nonlinear all-optical coherent generation and read-out of valleys in atomically thin semiconductors. *Small* **19**, 2301126 (2023).
37. Liu, G.-B., Xiao, D., Yao, Y., Xu, X. & Yao, W. Electronic structures and theoretical modelling of two-dimensional group-VIB transition metal dichalcogenides. *Chem. Soc. Rev.* **44**, 2643–2663 (2015).
38. Splendiani, A. et al. Emerging photoluminescence in monolayer MoS_2. *Nano Lett.* **10**, 1271–1275 (2010).
39. Nayak, P. K., Lin, F.-C., Yeh, C.-H., Huang, J.-S. & Chiu, P.-W. Robust room temperature valley polarization in monolayer and bilayer WS_2. *Nanoscale* **8**, 6035–6042 (2016).

40. Zhang, X. et al. Enhanced valley polarization of bilayer $MoSe_2$ with variable stacking order and interlayer coupling. *J. Phys. Chem. Lett.* **12**, 5879–5888 (2021).
41. Herrmann, P. et al. Nonlinear valley selection rules and all-optical probe of broken time-reversal symmetry in monolayer WSe_2. *Nat. Photon.* **19**, 300–306 (2025).
42. Aversa, C. & Sipe, J. E. Nonlinear optical susceptibilities of semiconductors: results with a length-gauge analysis. *Phys. Rev. B* **52**, 14636–14645 (1995).
43. Seith, A., Evers, F. & Wilhelm, J. Giant d.c.-like residual current generated by subcycle laser pulses. *Phys. Rev. Res.* **6**, 043149 (2024).
44. Klimmer, S. et al. Ultrafast coherent bandgap modulation probed by parametric nonlinear optics. Preprint at https://arxiv.org/abs/2504.06130 (2025).
45. Trivizas, G., Feinstein, M. D. & Almeida, E. Tuning coherent light generation in 2D semiconductors with strong laser fields. Preprint at https://arxiv.org/abs/2503.23613 (2025).
46. Bloembergen, N. Conservation laws in nonlinear optics. *J. Opt. Soc. Am.* **70**, 1429–1436 (1980).
47. van de Groep, J., Li, Q., Song, J.-H., Kik, P. G. & Brongersma, M. L. Impact of substrates and quantum effects on exciton line shapes of 2D semiconductors at room temperature. *Nanophotonics* **12**, 3291–3300 (2023).
48. Echeverry, J. P., Urbaszek, B., Amand, T., Marie, X. & Gerber, I. C. Splitting between bright and dark excitons in transition metal dichalcogenide monolayers. *Phys. Rev. B* **93**, 121107 (2016).
49. Yan, W. et al. Probing angle-dependent interlayer coupling in twisted bilayer WS_2. *J. Phys. Chem. C* **123**, 30684–30688 (2019).

Methods

Sample preparation and characterization

The mono- and multilayer WS_2 sample was mechanically exfoliated onto polydimethylsiloxane from a bulk crystal (HQ graphene), and then transferred onto a fused silica substrate. The different thicknesses (mono- and bilayer) were confirmed by PL and contrast measurements. For the PL measurements, we used a 532-nm diode laser (Cobolt 08-DPL 532 nm) as the excitation source, which we focus onto the sample with a ×50 objective (M Plan Apo 50x, Mitutoyo). The emitted PL was collected in reflection geometry and guided to the spectrometer (Horiba iHR550) after proper filtering with a longpass dichroic mirror (LPD02-532RU-25, Semrock) and a notch filter (FL532-3, Thorlabs).

Polarization-resolved THG

For all the THG experiments, we use a custom-built multiphoton microscope in transmission geometry. An optical parametric oscillator (Levante IR fs from APE), pumped by the output of an Yb-doped mode-locked laser (FLINT FL2-12, LIGHT CONVERSION) with a repetition rate of 76 MHz and a pulse length of ~100 fs, generates the FB, which is tunable in the range of 1,300–2,000 nm. To precisely control the pulse energy of the FB, we use a combination of a fixed Glan–Thompson polarizer (GTH10M, Thorlabs) and a wire grid polarizer (WP25M-UB, Thorlabs), which is mounted on a motorized rotation stage (PRM1/MZ8, Thorlabs). Subsequently, the ellipticity is controlled via a quarter-wave plate (RSU 2.4.15, B. Halle) mounted on another motorized rotation stage (PRM1/MZ8, Thorlabs). The FB is focused onto the sample by a ×40 mirror objective (LMM-40x-UVV) with a focal spot radius of 1.85 µm. The transmitted FB as well as the emitted TH are collimated by a lens (C330TMD, Thorlabs). To obtain the polarization-resolved results, we place another wire grid polarizer (WP25M-UB, Thorlabs) after the collimation and before the detector. We block the transmitted FB by two heat-absorbing filters (ISK171, Isuzu) as well as a shortpass filter (FESH0700, Thorlabs). Furthermore, bandpass filters for 610 nm (FBH610-10, Thorlabs) and 625 nm (87791, Edmund Optics) can be added. The TH signal is then detected by a silicon avalanche photodiode (APD440A, Thorlabs) and filtered by a lock-in amplifier (MFLI, Zurich Instruments) in combination with an optical chopper (MC2000B, Thorlabs) that modulates the FB at 971 Hz or by a single photon avalanche diode (SPAD, C22303-050, Hamamatsu) in combination with a counter (HM8123, Rohde & Schwarz).

Analytical methods

For the analytical calculation of the polarization-resolved THG, we use an analytical expression of the third-order NLO susceptibility[42]. Details are given in the Supplementary Sections 5 and 6.

Data availability

The data supporting the plots within this Article and the other findings of this study are available from the corresponding author upon reasonable request. Source data are provided with this paper.

Acknowledgements

S.S.S. thanks B. Dey and A. Slobodeniuk for their helpful discussions. This work was funded by the Deutsche Forschungsgemeinschaft (DFG, German Research Foundation) – Project-ID 398816777 – SFB 1375 (subproject C4); the International Research Training Group (IRTG) 2675 'Meta-Active', project number 437527638 (subproject A4); and the Federal Ministry for Education and Research (BMBF) project number 16KIS1792 SiNNER. J.W. acknowledges the DFG for funding via the Emmy Noether Programme (project number 503985532), CRC 1277 (project number 314695032, subproject A03) and RTG 2905 (project number 502572516).

Author contributions

F.F., P.H. and G.S. conceived the work. F.F. and P.H. performed the measurements and analysed the data. F.F., P.H. and G.S. interpreted the experimental results. S.K. fabricated the sample. S.S.S. and J.W. developed the analytical model. The manuscript was written with contributions from all co-authors.

Funding

Open access funding provided by Friedrich-Schiller-Universität Jena.

Competing interests

The authors declare no competing interests.

Additional information

Supplementary information The online version contains supplementary material available at https://doi.org/10.1038/s41566-025-01801-2.

Correspondence and requests for materials should be addressed to Giancarlo Soavi.

Peer review information *Nature Photonics* thanks Manfred Fiebig and Bernhard Urbaszek for their contribution to the peer review of this work.